Article

Wave Response of a Monocolumn Platform with a Skirt Using CFD and Experimental Approaches

Masaki Katafuchi [1] **, Hideyuki Suzuki** [1] **, Yuya Higuchi** [1] **, Hidetaka Houtani** [1] **and Edgard B. Malta** [2]
and Rodolfo T. Gonçalves [1,*]

1   OSPL-Ocean Space Planning Laboratory, Department of Systems Innovation, The University of Tokyo, Tokyo 113-8656, Japan
2   Technomar Engenharia Oceânica, São Paulo 05419-905, Brazil
*   Correspondence: goncalves@g.ecc.u-tokyo.ac.jp; Tel.: +81-3-5841-0480

Abstract: This paper aims to investigate the nonlinear motion characteristics of a monocolumn type floater with skirts numerically and experimentally. Wave calibration, free decay, and regular wave tests were simulated using a computational fluid dynamics (CFD) code OpenFOAM. The experiments were carried out in a wave tank to validate the CFD results. First, wave calibration tests were performed to investigate wave generation, development, propagation, and absorption in the numerical wave tank. Second, the simulation input parameters were calibrated to reproduce the waves generated in the tank experiment. Third, free decay tests of heave and pitch were conducted to examine the natural period and the linear and quadratic damping of the floater. A verification and validation study was performed using experimental data for free decay tests. Finally, regular wave tests were performed to investigate the motion characteristics of the floater. The results were processed to obtain the response amplitude operator (RAO) for the heave and pitch motions. The RAOs of the floater was compared with the experimental data and numerical simulations based on the linear potential theory code WAMIT to investigate the performance of the CFD simulations. The comparisons made in this work showed the potential of the CFD method to reproduce the motion characteristics of a shallow-draft floating object with a skirt in waves and to visualize the nonlinear phenomena behind the oscillation of the floating object.

Keywords: CFD; floater; nonlinear response; flow separation; fluid field

1. Introduction

The potential of offshore wind power in the exclusive economic zone of Japan is immense and is expected to be a great energy source in the future [1]. New government policies have been established to allow the long-term and exclusive use of general sea areas, supporting measures for wind condition surveys and the design and improvement of technical standards and operations [2,3].

While bottom-fixed type offshore wind turbines are in their commercial phase, floating offshore wind turbines (FOWTs) are in technological development. One of the reasons for this delay in development is the higher costs associated with the development of platforms or substructures. Since FOWTs oscillate by waves, large-draft platforms are used to support stability. These large platforms cannot be constructed with existing facilities and require their own. Therefore, the costs associated with the development of substructures and foundations occupy 27.1% of the total costs, while 8.4% in bottom-fixed type [4]. To overcome this shortcoming, many FOWT concepts with smaller drafts are introduced [5]. Most of these concepts are equipped with skirts or moonpools close to the water plane to reduce their motion in waves. However, this equipment makes the prediction of motion characteristics by simulation methods based on the linear potential theory difficult.

Advanced-Spar type FOWT, one of the platform concepts for FOWT, is characterized by its two footing structures [6,7] (see Figure 1). Performances of various concepts of monocolumn platforms under waves have been investigated in many studies. Gonçalves et al. (2008, 2010) [8,9] studied the influence of appendages on a monocolumn platform under waves by model tests. Wang et al. (2016) [10] and Du et al. (2018) [11] analyzed RAOs of a sand-glass type floating body and modeled the nonlinearity in heave motion. Amin et al. (2020) [12] conducted model tests to investigate RAOs of a floating desalination plant under a range of wave heights and frequencies. They compared the results with numerical solutions from a frequency domain program. Rao et al. [13] confirmed nonlinear damping in free decay tests of heave for similar platforms, and Jang et al. [14] showed the existence of nonlinear hydrostatic restoration stiffness due to the nonuniform water plane area for the Arctic Spar model. Numerical simulations of the motion of floating platforms in waves are of great importance in their design phase. In response to the limitation of the potential theory calculation, alternative simulation methods have been developed.

Figure 1. The conceptual idea of the Advanced Spar FOWT.

Computational fluid dynamics (CFD) simulations of motion prediction for FOWT concepts have been increasingly attempted to compute the viscous effects ignored in the potential theory. Beyer et al. (2013) [15] simulated free decay in surge, and Quallen and Xing (2016) [16] predicted the motion under wind and waves, both for the OC3-Hywind spar-type wind turbine. Borisade et al. (2016) [17] predicted the motion of the IDEOL Floatgen platform under a regular wave condition, and Xue et al. (2022) [18] simulated a semisubmersible FOWT with a tuned liquid multicolumn damper for several regular wave conditions. The pitch decay motion and motion under several regular wave conditions of the OC5 DeepCwind semisubmersible FOWT were simulated by Wang et al. (2019,

2020) [19,20] . Although these studies accurately predicted the validation data, the number of incident waves was too small to understand the motion characteristics of the target floating structures.

Suzuki et al. [21] studied the hydrodynamic mechanism behind the nonlinear motion behavior of a monocolumn platform with a skirt, as shown in Figure 2. They confirmed the suppressed RAO for heave and pitch in high-height waves by CFD simulation. They compared the simulation data with the towing tank experiment and showed qualitatively good agreement. However, the study had not followed the verification and validation (V&V) procedure or systematic grid generation. Moreover, apparent discrepancies between the simulation and the experimental results were observed around the resonance period.
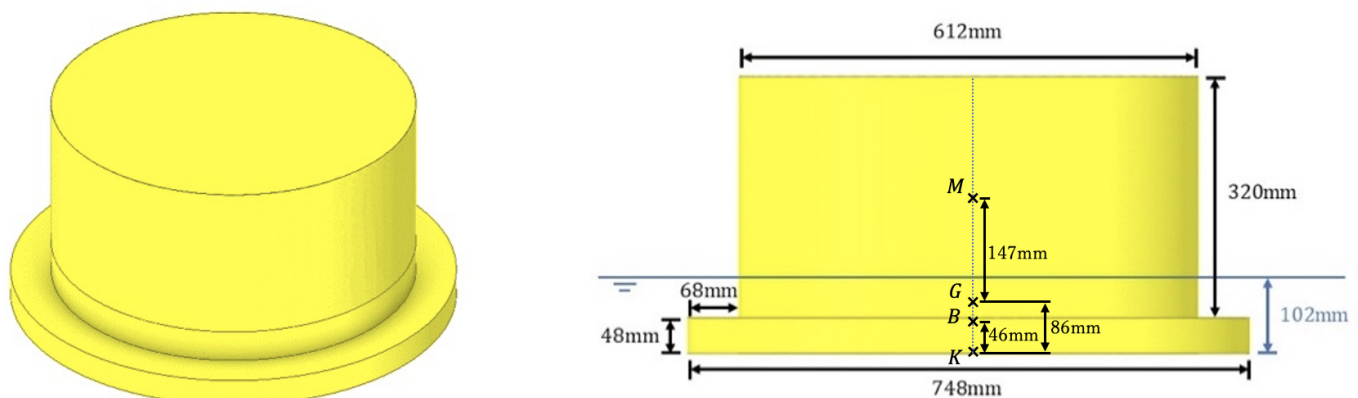

Figure 2. Dimensions of the reduced-scale model of the floater.

This study aims to reproduce the nonlinear motion characteristics of the floater with a skirt in waves more accurately by using CFD. OpenFOAM v-1812 was used to simulate the oscillation of the floater shown in Figure 2 under various regular wave conditions. Wave calibration, free decay, and regular wave tests were performed both experimentally and numerically and RAOs were compared. Regular wave tests were also performed by WAMIT, a simulation code based on linear potential theory, to show improvements in CFD simulations. This paper starts with a description of the experiment. Then, the details of the numerical settings in OpenFOAM are presented. The results of the regular wave test simulation are validated using the response amplitude operator (RAO) of the experimental data and discussed. Finally, conclusions are drawn from the discussions.

2. Experimental Setups

2.1. Reduced Scale Floater Model

The floater studied on the real scale was a cylindrical floater with a diameter of 45 m. The footing had a diameter of 55 m and a thickness of 3.5 m. The draft of the floater was 7.5 m. The reduced-scale model of the floater used in the experiments and CFD simulations was a 1/73.5 scale model, as shown in Figure 2. The floater had a freeboard that was high enough to prevent over-topping by waves. The positions of the center of gravity and the metacenter were adjusted to take into account the structures removed, such as the rotor nacelle assembly (RNA), the tower, and the bottom footing. However, in this study, the thrust that acts on the RNA or the tower was not considered because the effect of the skirt near the free surface was of interest. The main properties of the floater are presented in Table 1.

Table 1. Main properties of the floater.

Property	Value
Displacement [kg]	36.96
KG [mm]	86
BM [mm]	187
KB [mm]	46
GM [mm]	147
Pitch Radius of Gyration [mm]	215

2.2. Wave Tank

All experiments were carried out in a towing tank at UTokyo, the University of Tokyo, Japan, with 85.0 m × 3.5 m × 2.4 m (length × width × depth). The experimental setup views are illustrated in Figure 3.

In wave calibration tests, the wave height was measured for all incident waves shown in Table 2. The wave height 2.72 cm corresponds to 1 m in the full scale, which is small, and the nonlinear effect is negligible. Measurements 6.80 cm and 13.6 cm correspond to 2 m and 5 m in full scale, where a remarkable nonlinear behavior of the floater is expected. The wave period range in the table corresponds to 7.0 through 16.5 s in the full scale, which is derived from the actual range of periods for actual sea conditions. A servo-type wave height gauge was installed in the middle of the 85-m-long water tank, 40 m from the wave generator, to observe the surface elevation.

In the free decay and regular wave tests, the floater was positioned at the same position where the wave height gauge was installed in the wave calibration tests. It used a combined system of gimbals and a heave rod. The 6DOF motions of the floater were measured using both potentiometers and the Qualysis Optical Motion Capture System with 4 cameras. The data from the potentiometers were used for the analysis. A picture of the floater under regular wave tests is shown in Figure 4.
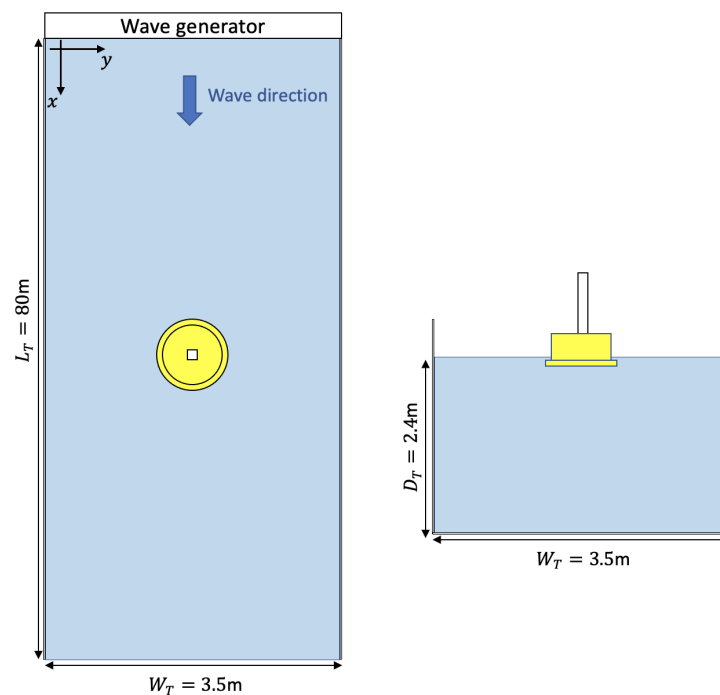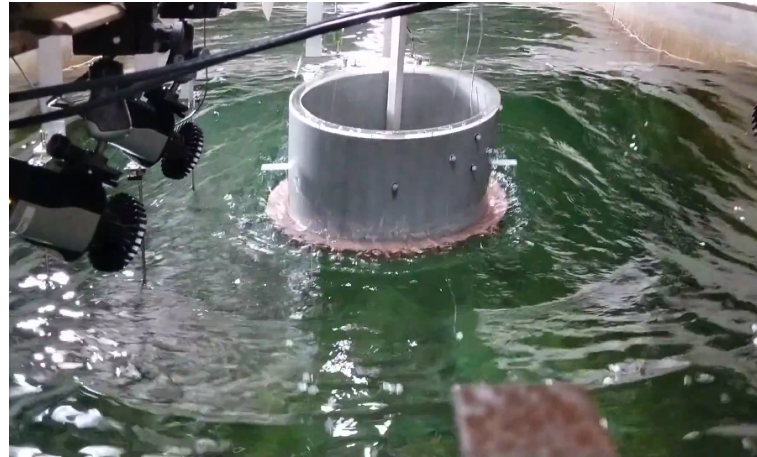

Figure 3. Top and front views of the wave tests setup in the towing tank.

Table 2. List of incident waves.

Wave Height [cm]	Period Range [s]
2.72	0.8, 0.9..., 1.9
6.80	1.0, 1.1..., 1.9
13.6	1.3, 1.4..., 1.9

Figure 4. Picture of the reduced scale model during regular wave tests in the towing tank.

3. Numerical Settings

3.1. Governing Equations

In the CFD study, the URANS equations for an incompressible fluid were solved. The URANS equations are given by:

$$\frac{\partial \rho U_i}{\partial x_i} = 0,\tag{1}$$

$$\frac{\partial \rho U_i}{\partial t} + \frac{\partial}{\partial x_j}\left(\rho U_i U_j + \rho \overline{u_i' u_j'}\right) = -\frac{\partial P}{\partial x_i} + \frac{\partial}{\partial x_j}\left[\mu\left(\frac{\partial U_i}{\partial x_j} + \frac{\partial U_j}{\partial x_i}\right)\right] + f_{\sigma i}.\tag{2}$$

In the above equations, ρ is the fluid density, U_i and u' denote the time average components of the fluctuating components of the velocity, while p and p' denote the fluctuating components of the pressure, respectively. μ is the kinematic viscosity. Surface tension $f_{\sigma i}$ is given by:

$$f_{\sigma i} = \sigma \kappa \frac{\partial \alpha_1}{\partial x_i},\tag{3}$$

where α_1 is the volume of fraction, σ is the surface tension constant, and κ is the curvature modeled as follows:

$$\kappa = -\frac{\partial}{\partial x_i}\left(\frac{\partial \alpha_1 / \partial x_i}{|\partial \alpha_1 / \partial x_i|}\right).\tag{4}$$

3.2. Turbulence Modeling

The last term on the right-hand side of Equation (2), $\tau_{ij} = -\rho \overline{u_i' u_j'}$, is called the Reynolds stress tensor and is modeled as follows:

$$\tau_{ij} = \mu_t\left(\frac{\partial U_i}{\partial x_j} + \frac{\partial U_j}{\partial x_i}\right) - \frac{2}{3}\rho \delta_{ij} k - \frac{1}{3}\delta_{ij}\frac{\partial U_k}{\partial x_k},\tag{5}$$

where δ_{ij} is the Kronecker delta, μ_t is the turbulent kinematic viscosity, and k is the turbulent kinetic energy. The transport equation for k is solved to close the system of equations. In

the $k - \omega$ SST-SAS model proposed by Menter and Egorov(2007) [22], transport equation for k is given by:

$$\frac{\partial k}{\partial t} + U_j \frac{\partial k}{\partial x_j} = P_k - \beta^* k \omega + \frac{\partial}{\partial x_j} \left[(\nu + \sigma_k \nu_T) \frac{\partial k}{\partial x_j} \right] \tag{6}$$

accompanied by the transport equation of the specific dissipation rate ω:

$$\frac{\partial \omega}{\partial t} + U_j \frac{\partial \omega}{\partial x_j} = \alpha S^2 - \beta \omega^2 + \frac{\partial}{\partial x_j} \left[(\nu + \sigma_\omega \nu_T) \frac{\partial \omega}{\partial x_j} \right] + 2(1 - F_1) \sigma_{\omega 2} \frac{1}{\omega} \frac{\partial k}{\partial x_i} \frac{\partial \omega}{\partial x_i} + Q_{SAS}. \tag{7}$$

See Menter and Egorov [22] for details.

Burmester et al. (2020) [23] found that the KSKL model, which can be transformed to the $k - \omega$ SST-SAS model [24] and available in OpenFOAM, is favored for the decaying motion of floating structures compared to some other models and laminar simulation.

3.3. Volume of Fluid Method

Since the computational domain includes two phases—water and air—the Volume of Fluid (VOF) method was used to capture the free surface. The volume of fraction α_1 of water in a cell is introduced to calculate the physical properties that appear in Equation (2) as:

$$\rho = \alpha_1 \rho_{water} + (1 - \alpha_1) \rho_{air}, \tag{8}$$

$$\mu = \alpha_1 \mu_{water} + (1 - \alpha_1) \mu_{air}. \tag{9}$$

To determine the interface of two fluids, an additional transport equation for α_1:

$$\frac{\partial \alpha_1}{\partial t} + \frac{\partial (\alpha_1 u_j)}{\partial x_j} = 0, \tag{10}$$

was solved.

3.4. Discretization and Solution Process

The volume integral of the continuity Equation (1), the momentum Equation (2), and the transport Equations (6), (7) and (10) were discretized using the following schemes. For all of the above equations, the time derivatives were discretized by the Euler method and the face values were obtained by linear interpolations. For the momentum Equation (2), the linear upwind scheme was used for the convection term, and the linear scheme with the over-relaxed approach was used for the diffusion term. For the turbulent transport Equations (6) and (7), the linear upwind scheme with gradient limiters was used for the convection terms. For the transport equation for α_1 Equation (10), the van Leer scheme was used for the convection term.

The PIMPLE algorithm with 2 inner loops and 1 non-orthogonal corrector loop was used to couple the discretized URANS Equations (1) and (2).

3.5. Mesh Generation

The numerical wave tank was generated by the *blockMesh* utility of OpenFOAM to reproduce the towing tank at UTokyo. Since incident waves propagate in the x direction, the sway, roll, and yaw motions of the floater are negligible due to the symmetry in the XZ plane. Therefore, the computational domain was reduced to half of the entire domain. Furthermore, the domain was reduced in the x direction to 7 times the wavelength of the incident wave + floater length, as shown in Figure 5, because the numerical domain was sufficient for wave development and wave absorption.
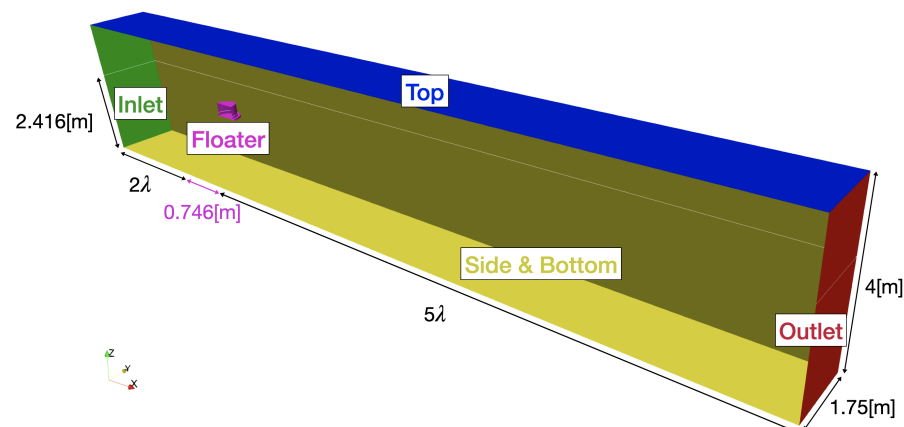
Figure 5. Schematic view of the computational domain.

The numerical domain was divided into cells by the following rules.

- For the *x* direction, the length of each cell was set at 1/20 of the incident wavelength.
- For the *y* direction, the domain was divided into 20 cells regardless of the incident wave.
- For the *z* direction, the domain was divided into seven layers: FSL (Free Surface Layer), GL1U (Grading Layer 1st Upper), GL1L (Grading Layer 1st Lower), CLU (Constant Layer Upper), CLL (Continuous Layer Lower), GL2U (Grading Layer 2nd Upper) and GL2L (Grading Layer 2nd Lower).
  - FSL covered the free surface. This layer had a height of 1.3 times the wave height of the incident wave and was divided into 14 cells.
  - GL1U was generated only for H = 2.72 cm and 6.8 [cm]. The top of this layer was 1.3 times 6.8 [cm] (1/2 of the highest wave height) above the free surface. The height of the bottom cell was set to 2.0 times the height of the FSL cell. The height of the top cell was five times the height of the lowest cell, and the heights of the intermediate cells expanded in a constant ratio.
  - GL1B was generated only for H = 2.72 cm and 6.8c m. The bottom of this layer was 1.3 times 6.8 [cm] (1/2 of the highest wave height) below the free surface. The height of the top cell was set at 1.5 times the height of the FSL cell. The height of the bottom cell was 0.15 times the height of the lowest cell, and the intermediate cells were expanded in a constant ratio.
  - CLU covered the motion range of the floater. The top of this layer was set to the freeboard height of the floater + the incident wave height times 1.2 times the maximum heave RAO observed in the experiments above the free surface. The height of the cells in this layer was set to 2.0 times the height of the FSL cells for H = 1.36 cm.
  - CLB covered the motion range of the floater. The bottom of this layer was set to the draft of the floater + the incident wave height times 1.2 times the maximum heave RAO observed in the experiments below the free surface. The height of the cells in this layer was set to 2.0 times the height of the FSL cells for H = 1.36 cm.
  - GL2U covered the remaining region above the free surface. The height of the bottom cell was set to 2.0 times the height of the CLU cell. The height of the top cell was five times the height of the bottom cell, and the heights of the intermediate cells were expanded with a constant ratio.
  - GL2B covered the remaining region below the free surface. The height of the top cell was set to 1.5 times the height of the CLB cell. The height of the bottom cell was 6.67 times the height of the top cell, and the intermediate cells were expanded with a constant ratio.

The mesh around the floater was further refined in the x and y directions using the OpenFOAM utility *refineMesh*. The mesh for the floater was generated from an STL file with the help of *snappyHexMesh*. The generated mesh is shown in Figures 6–8.
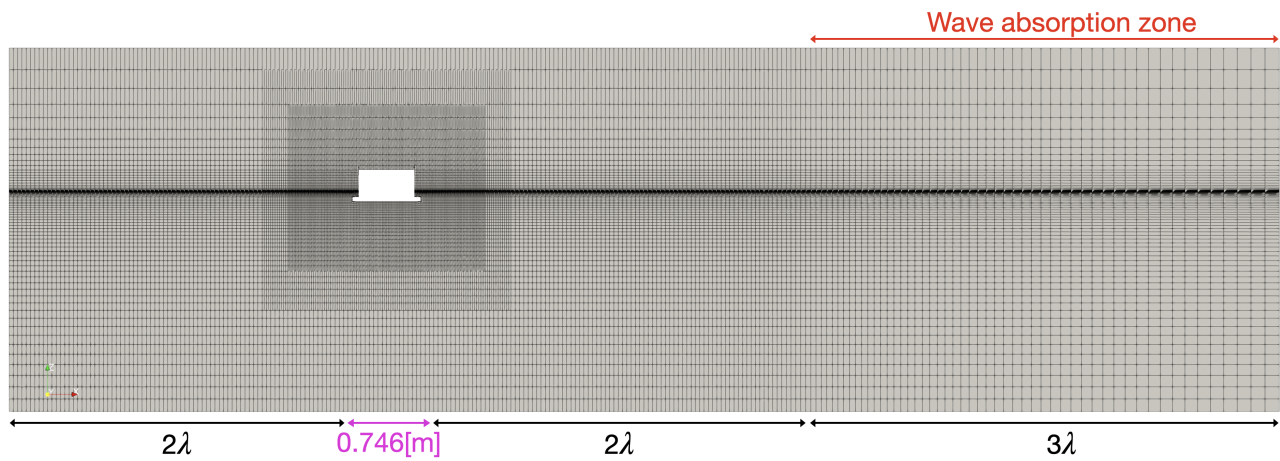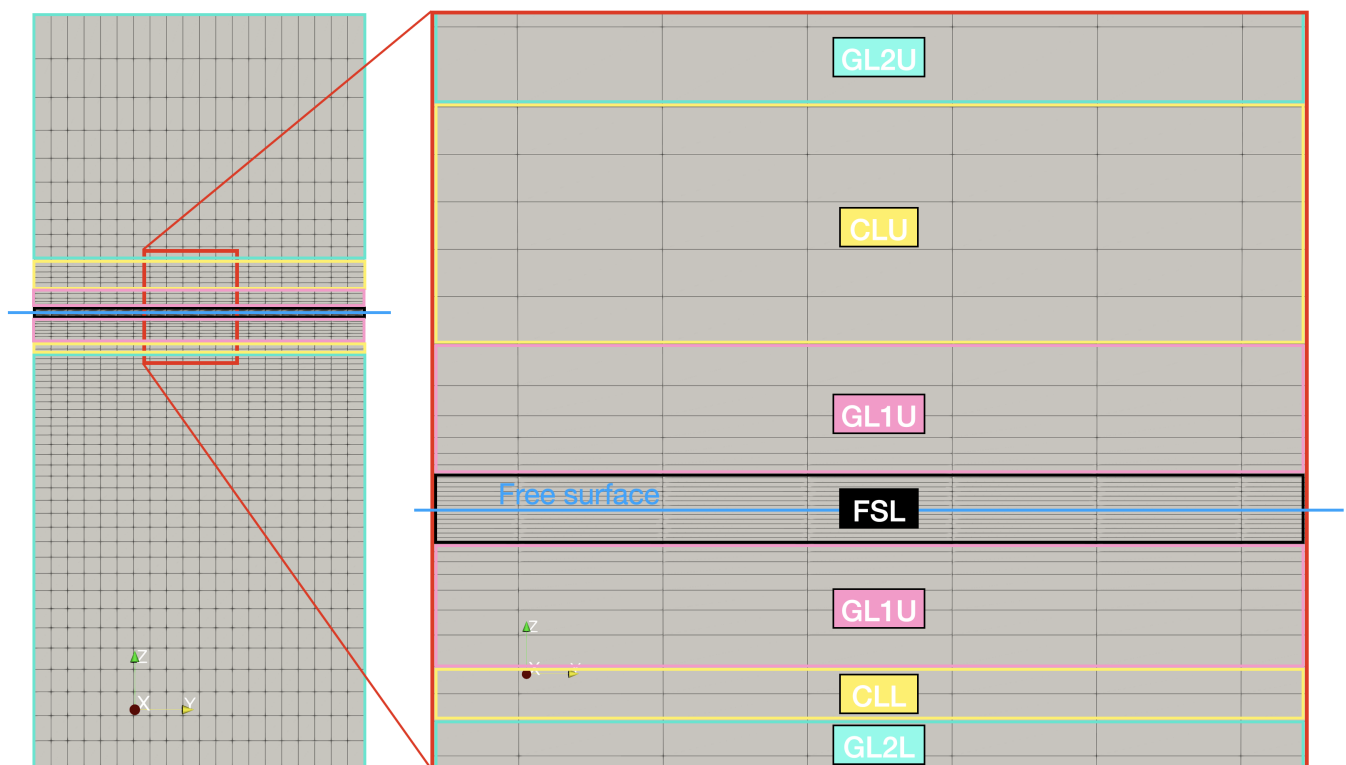

Figure 6. Generated mesh of the middle plane.

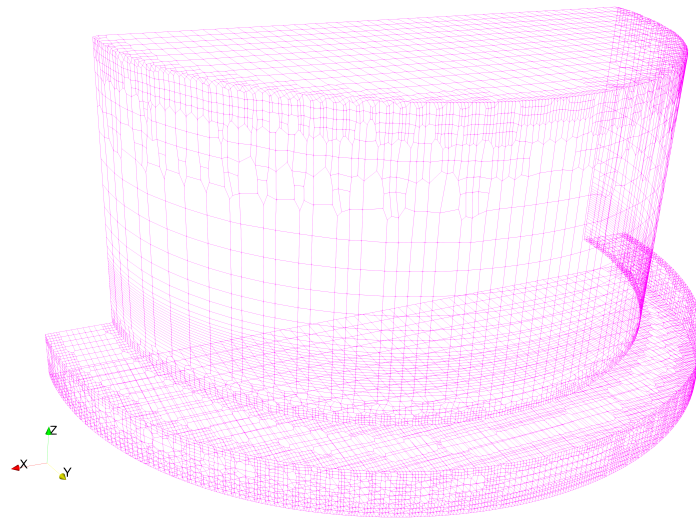**Figure 7.** Generated mesh of the inlet patch.

Figure 8. Generated mesh of the floater.

3.6. Boundary Conditions

Symmetry conditions were applied to the middle plane and Side and Bottom patches. Regarding the floater patch, the moving qall velocity condition for velocity, the fixed flux pressure condition for pressure, the zero gradient condition for α_1 and the wall functions for k and ω, respectively, were applied. Other boundary conditions and prescribed values are listed in Table 3.

Table 3. Boundary conditions and prescribed values for the inlet, outlet, and top patches.

Variable	Inlet	Outlet	Top
U_i	Wave Velocity	Wave Velocity	Pressure Directed Inlet-Outlet Velocity, 0
$P - \rho g h$	Fixed Flux Pressure	Fixed Flux Pressure	Total Pressure, 0
k	Fixed Value, 1.0×10^{-5}	Inlet-Outlet, 1.0×10^{-5}	Inlet-Outlet, 1.0×10^{-5}
ω	Fixed Value, 2	Inlet-Outlet, 2	Inlet-Outlet, 2
α_1	Zero Gradient	Zero Gradient	Inlet-Outlet, 0

3.7. Dynamic Mesh

Since we investigate the motion of the floater caused by waves, the dynamic mesh technique was applied to the mesh region close to the floater patch. The floater's part of the computational domain was regarded as a rigid body and moved in accordance with the force exerted. The Newmark-beta method was used to numerically solve the equation of rigid body motion. Cells within the inner distance of the floater patch are moved directly as a rigid body attached to the floater patch. Other cells within the outer distance were morphed. In this study, the inner distance was set at 0.02 m and the outer distance at 2.0 m.

3.8. Time Step and Simulation Time

The CFD simulation time steps were set to 0.002 s. The simulation times for the wave calibration tests were 40 times the period of the incident waves. Shorter simulation times were used for free decay tests because the experiments showed strong damping in both motion modes. The simulation times for the free decay tests were 11 s for the heave and 25 s for the pitch. For regular wave tests, the simulation times were 35 times the period of the incident waves. Simulation times were prolonged in regular wave tests when the response was not stable.

3.9. WAMIT Settings

In WAMIT simulations, the external damping due to the viscous effects must be included as an external linear matrix to compute the RAOs of the floater. Simulations were performed with two different damping; the percentage of critical damping obtained by experimental free decay tests and the CFD simulations. Both results are compared with the regular wave tests.

4. Results and Discussions

4.1. Wave Calibration Tests

For all cases, stable surface elevations were observed regardless of the wave height and period of the input wave. Figure 9 shows the time series of $H = 13.6$ [cm] and $T = 1.5$ [s] obtained by CFD simulation and the theoretical value of the third-order Stokes wave in deep water.
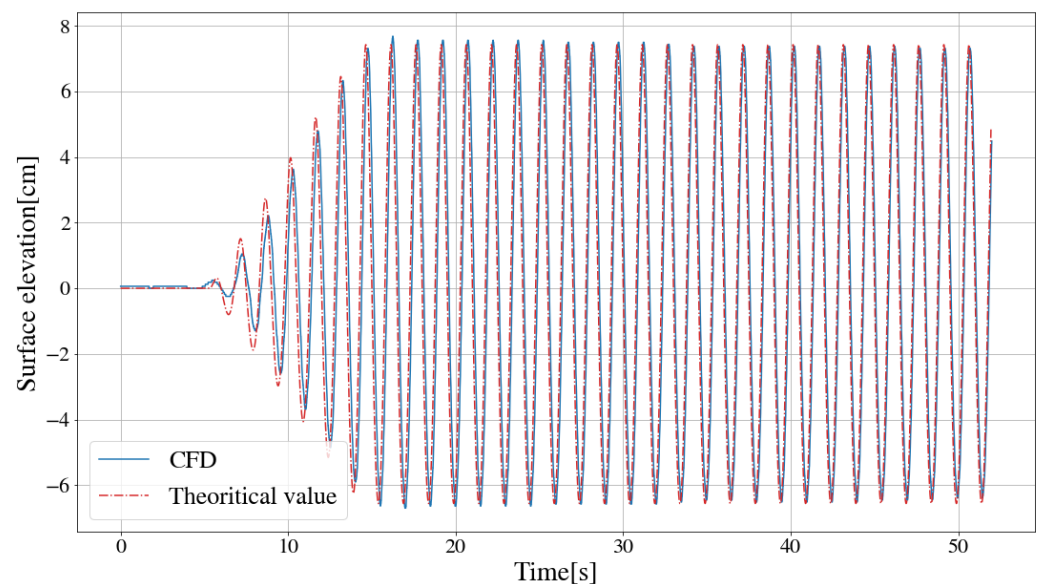

Figure 9. Time series of a wave calibration test $H = 13.6$ cm and $T = 1.5$ s.

For wave calibration tests, the wave height was computed from the root mean square (RMS) of the time series in both the experiments and the CFD simulations. The input wave heights for the CFD were modified to reproduce the same waves as possible as in the experimental cases. The results of the experiments and the CFD are compared in Figure 10. The wave calibration tests produced stable wave forms and the error in wave height of the experiment was reduced to less than 1% in all cases.

4.2. Free Decay Tests

Figures 11 and 12 show the comparison of the time series of the motion of the floater. As can be seen in the figures, the CFD simulations reproduced the experimental results with reasonable accuracy. However, stronger attenuations were observed in the experiments for both motions.

To make the qualitative comparison, three properties, the natural period T_n, the linear damping coefficient ζ, and the quadratic damping coefficient $B_2/(M + A)$, were investigated. These properties were determined from time series using the procedures presented in Appendix A. Convergence studies were conducted for these properties as well. For each degrees of freedom, five different combinations of typical cell size and time step, shown in Tables 4 and 5, were used.
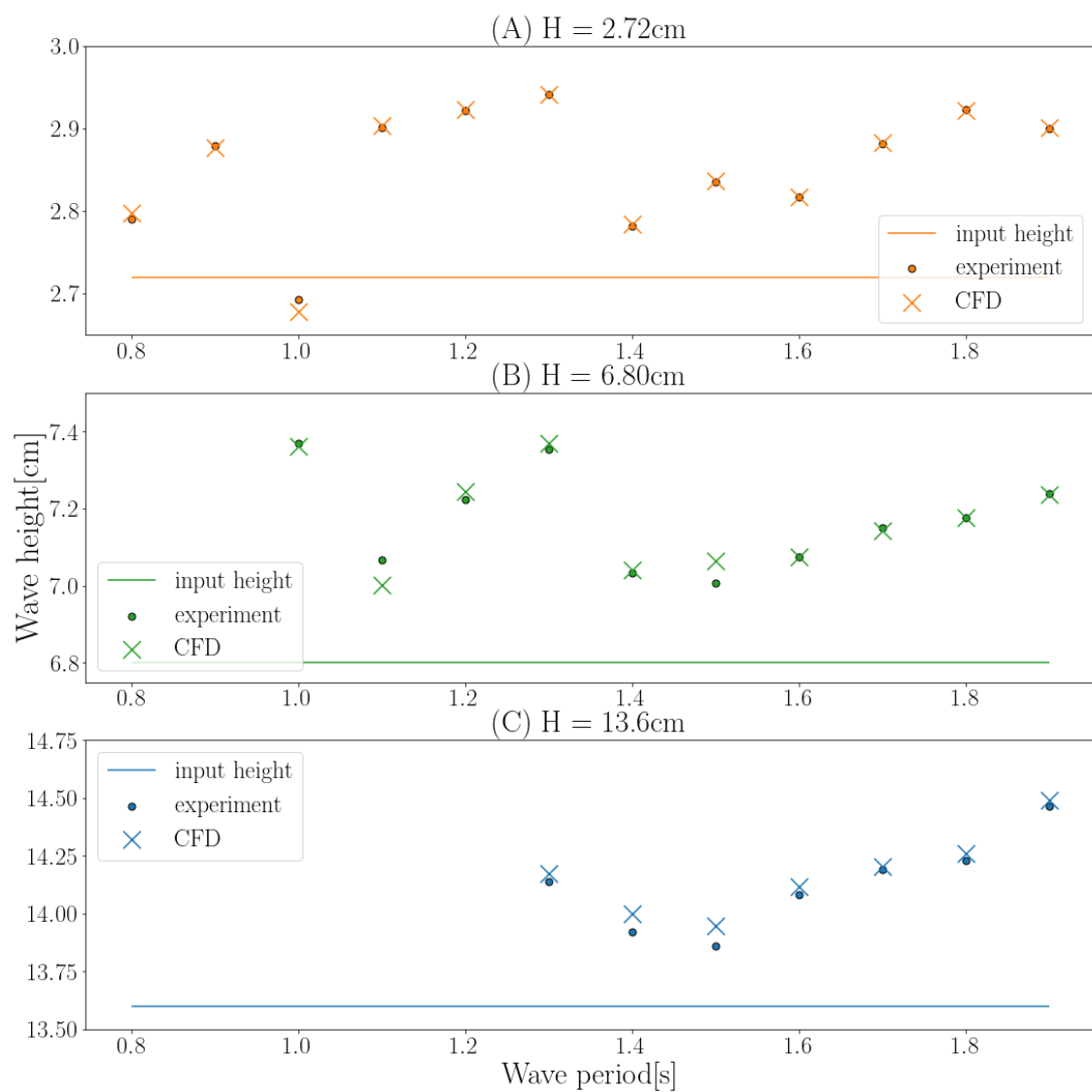
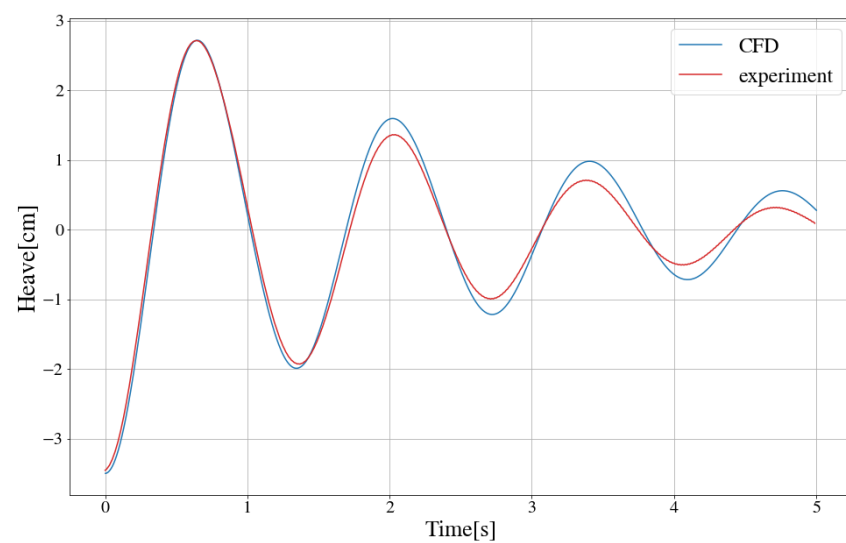**Figure 10.** Wave height obtained from RMS of the time series.

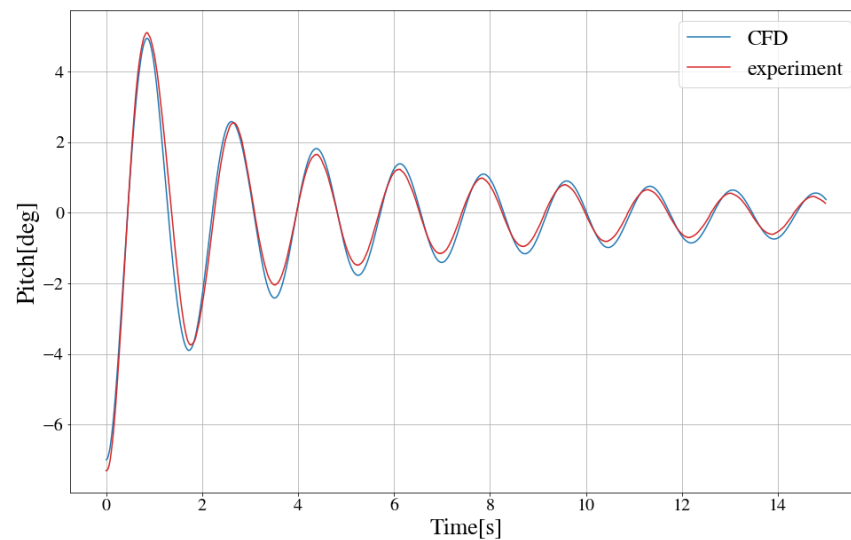**Figure 11.** Time series of the free decay test of heave.

Figure 12. Time series of the free decay test of pitch.

Table 4. Combinations of typical cell size and time steps used in the free decay test of heave.

Symbol	Comb.1	Comb.2	Comb.3	Comb.4	Comb.5
Typical Cell Size [m^3]	2.33×10^{-4}	3.10×10^{-4}	4.77×10^{-4}	2.33×10^{-4}	2.33×10^{-4}
Time Step [s]	1.00×10^{-3}	1.00×10^{-3}	1.00×10^{-3}	1.41×10^{-3}	2.00×10^{-3}

Table 5. Combinations of typical cell size and time steps used in the free decay test of pitch.

Symbol	Comb.1	Comb.2	Comb.3	Comb.4	Comb.5
Typical Cell Size [m^3]	2.33×10^{-4}	3.10×10^{-4}	4.77×10^{-4}	2.33×10^{-4}	2.33×10^{-4}
Time Step [s]	2.83×10^{-3}	2.83×10^{-3}	2.83×10^{-3}	4.00×10^{-3}	5.66×10^{-3}

The results are shown in Tables 6 and 7. In the tables, *Comparison Error* is the absolute value of the difference between the experiment and CFD simulation and *Validation Uncertainty* U_v is given by:

$$U_v = \sqrt{U_{num}^2 + U_{exp}^2}, \tag{11}$$

where U_{num} is the numerical uncertainty and U_{exp} is the experimental uncertainty. Numerical uncertainties were determined using generalized Richardson extrapolation and correction factor presented in the ITTC guidelines(2017) [25], and the Student-t distribution based method was used to obtain experimental uncertainties following the procedures in Rosetti (2015) [26].

Table 6. Comparison of the free decay test results for heave from experiments and CFD simulations using the quadratic method.

Property	Experiment	CFD	Comparison Error	Validation Uncertainty
$T_{n,3}$ [s]	1.378	1.382	0.004	0.006
$B_{2,33}/(M_{33} + A_{33})$ [m^{-1}]	0.016	0.025	0.003	0.048
ζ_3 [%]	9.147	6.561	2.585	3.223

Table 7. Comparison of the free decay test results for pitch from experiments and CFD simulations using the quadratic method.

Property	Experiment	CFD	Comparison Error	Validation Uncertainty
$T_{n,5}$ [s]	1.735	1.737	0.002	0.004
$B_{2,55}/(M_{55} + A_{55})$ [deg^{-1}]	0.070	0.059	0.011	0.014
ζ_5 [%]	0.573	0.472	0.102	2.118

As shown in the tables, the results of the CFD simulation showed good convergences for each degrees of freedom and the differences were smaller than the corresponding validation uncertainties for the combinations presented in Tables 4 and 5. Differences between CFD results and experimental data can be explained by damping levels. The CFD results agree very well qualitatively; however, there are some quantitative differences—mainly for heave motion. The difference is due to the calculation of viscous effects and vortex-shedding effects around the skirt, as can be seen in Figures 11 and 12. Moreover, the CFD calculations underestimated the damping levels for all degrees of freedom.

To examine the effect of damping, the extinction curves of the free decay tests of both degrees of freedom are shown in Figures 13 and 14. For heave, the decrements were large throughout the time series and strong attenuation was observed in the time series shown in Figure 15. On the other hand, for pitch, the decrement has decreased as time elapsed. Interestingly, the slope of the regression line, which corresponds to the quadratic damping coefficient $B_2/(M + A)$, is greater for pitch. The difference is clearly shown in Figures 15 and 16, which illustrate the time series as quadratic and linear fit curves. While fitted curves are almost the same for heave, the quadratic and linear fitted curves show significant discrepancy for pitch.
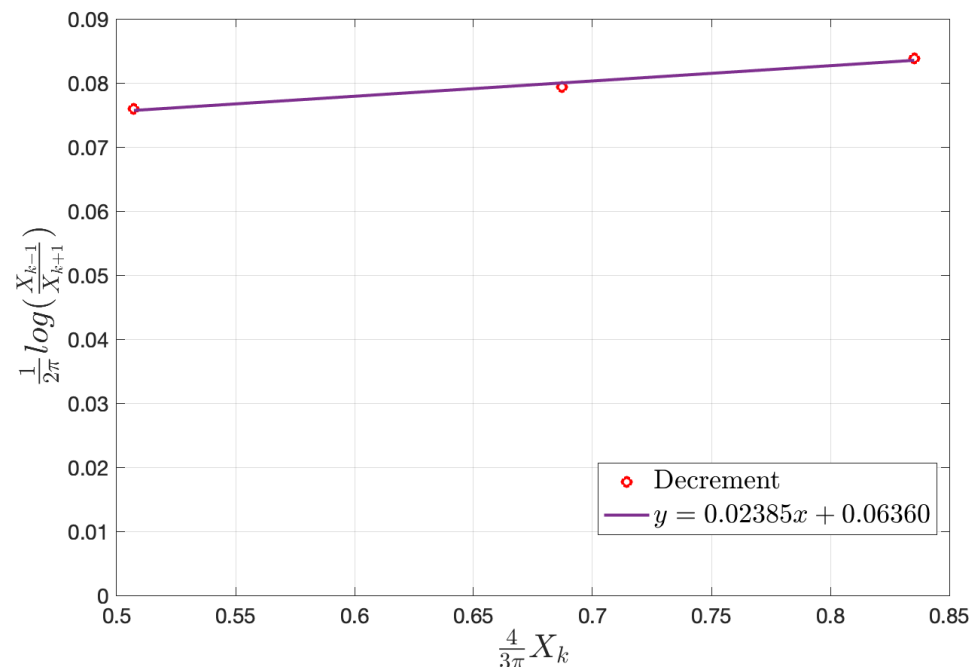
Figure 13. Extinction curve for the free decay test of heave obtained from CFD simulation with Comb.1.
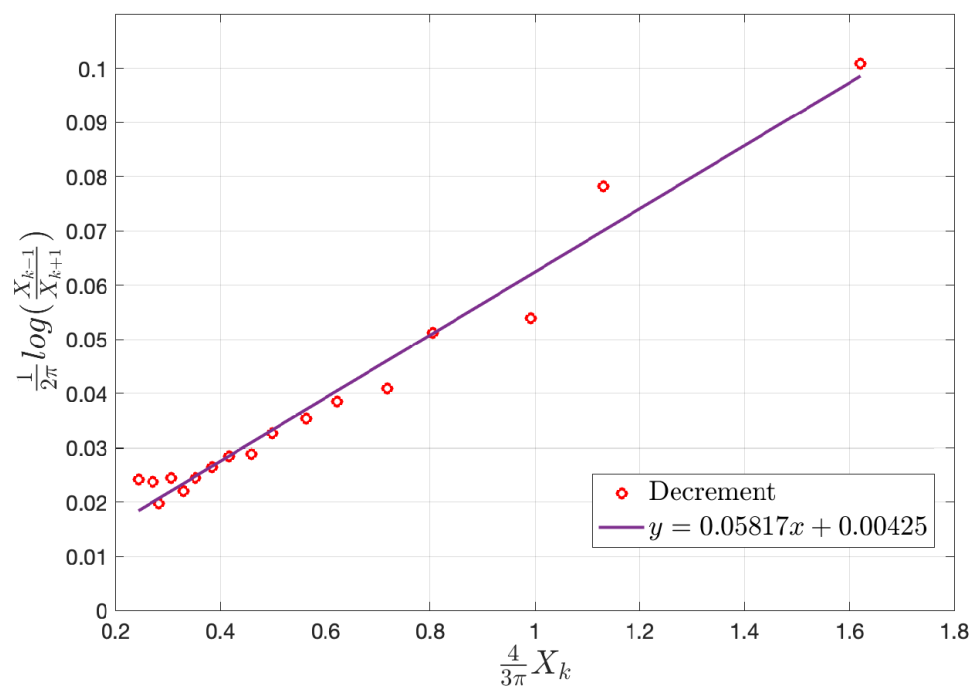
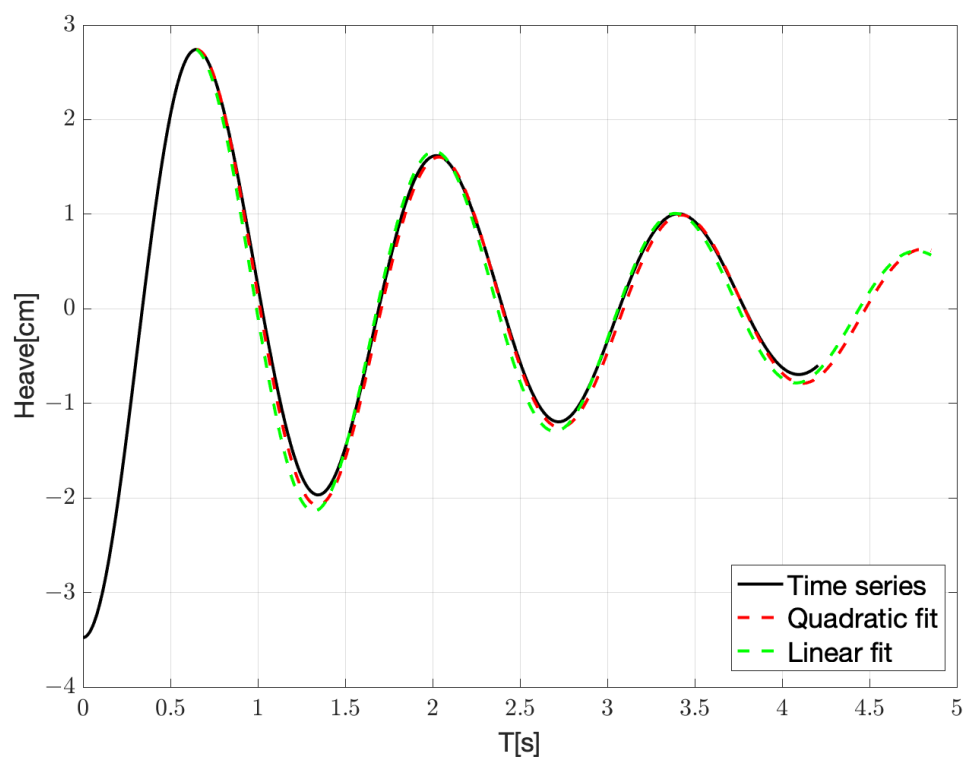**Figure 14.** Extinction curve for the free decay test of pitch obtained from CFD simulation with Comb.1.

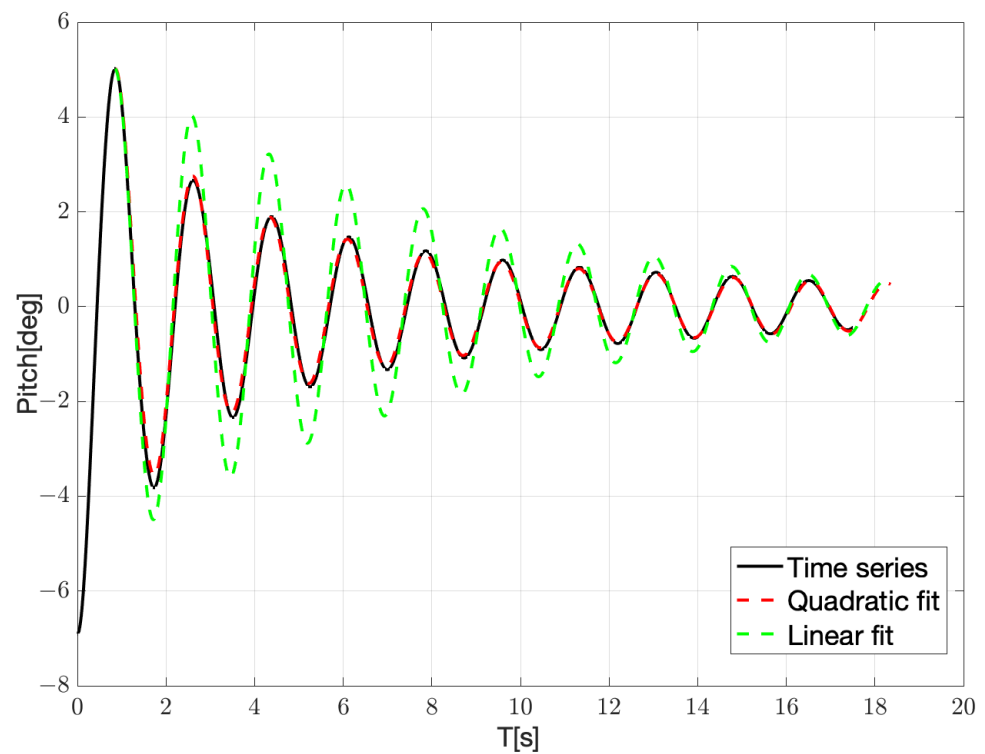**Figure 15.** Time series and fit curves of the free decay test of heave obtained from CFD simulation with Comb.1.

Figure 16. Time series and fit curves of the free decay test of pitch obtained from CFD simulation with Comb.1.

4.3. Regular Wave Test

The amplitude of the response was calculated from the RMS of the time series in both heave and pitch motions. Then the amplitude was nondimensionalised by the results from the wave calibration tests. The RAOs obtained from the CFD simulations are plotted together with the data from the experiments and simulations by WAMIT in Figures 17 and 18.
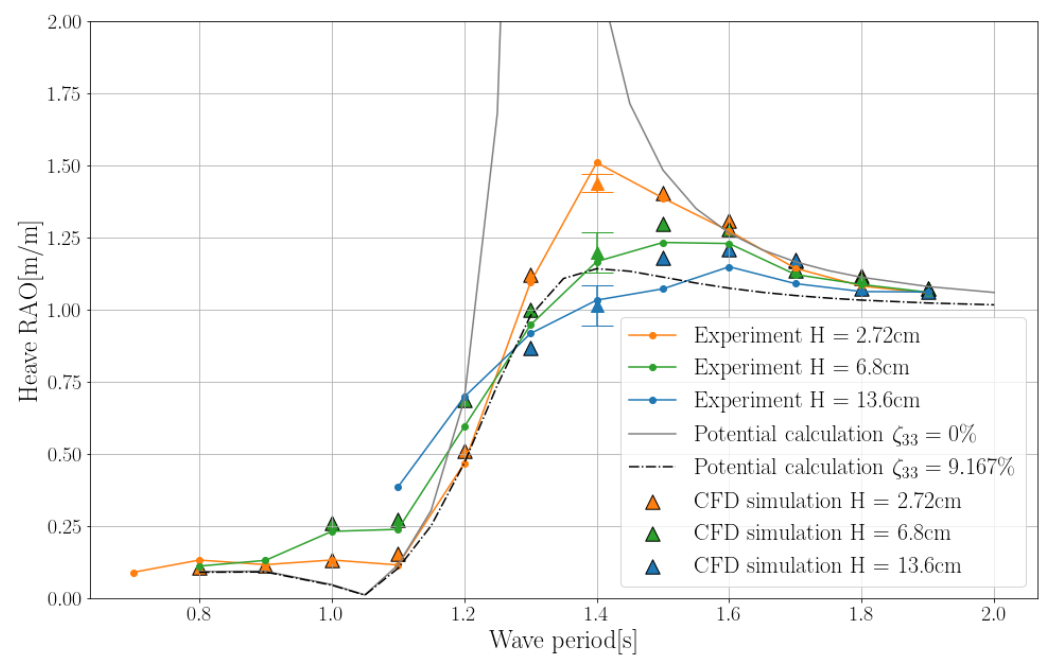

Figure 17. RAO of the heave motion of the floater in waves.
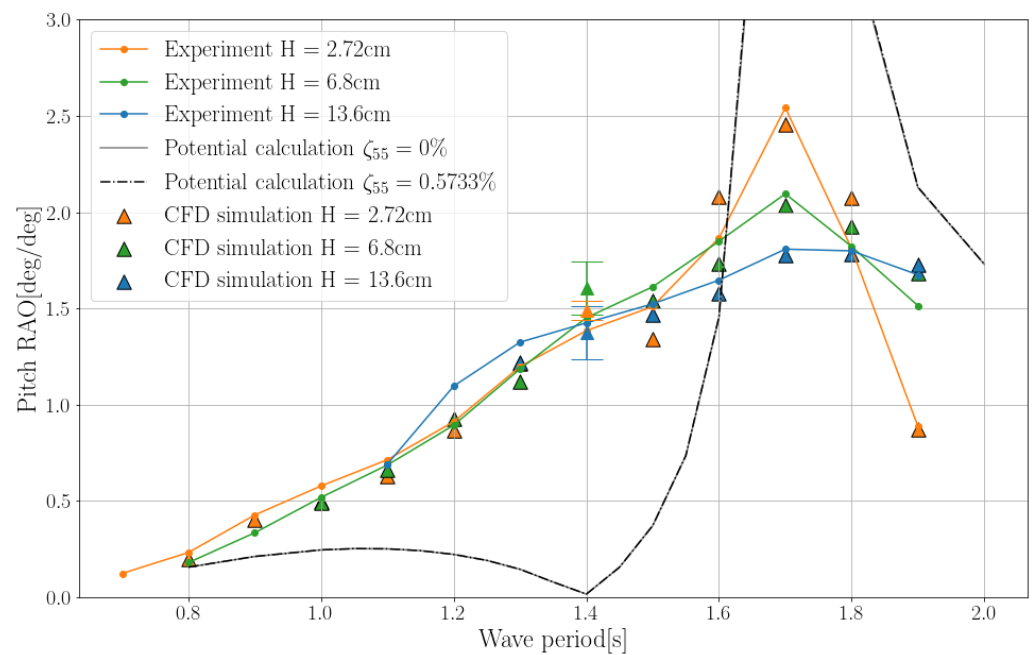
Figure 18. RAO of the pitch motion of the floater in waves.

The figures show good agreement between the experiments and the CFD simulations in both degrees of freedom at all incident wave heights. Furthermore, the peak periods of each wave height computed by the CFD simulations coincided with the experimental data. The bars shown at $T = 1.4$ s are the numerical uncertainties calculated with the same procedure as in Section 4.2. Since the experiment was not repeated for each case, the experimental uncertainties were not taken into account. However, the CFD simulations showed convergence in the close values of the corresponding experimental cases.

For the heave RAOs, as illustrated in Figure 17, WAMIT simulations without viscous damping ($\zeta_{33} = 0$) showed much higher RAOs for wave periods close to the natural period $T \approx 1.4$ s. This implies that there exist significant nonlinear effects even for the cases with a small incident wave height $H = 2.72$ cm if the wave period is close to the natural period. Nonlinear effects that reduce the RAO values of the heave motion near $T \approx 1.4$ s can be attributed to nonlinear damping due to flow separations occurring at the skirt, which is not considered in WAMIT simulations, due to the reason presented below.

First, the results of the experiments and the CFD simulation illustrated in Figure 17 show the smaller RAOs for the larger wave height for $T = 1.3$ s and greater. This suggests that nonlinear damping exists and increases as the response amplitude become greater. The CFD flow visualization shows larger-scale flow separations in cases with high wave heights. Figures 19 and 20 show the magnitude of the vorticity computed in the closest meshes to the plane $y = 0$ near the skirt of the floater at $T = 1.4$ s with $H = 2.72$ cm and $H = 13.6$ cm, respectively. While flow separations at the skirt are clearly shown in Figure 20, no notable flow separation is shown in Figure 19. This contrast suggests the existence of nonlinear damping due to the flow separations, which might result in smaller RAOs in cases with high wave heights.
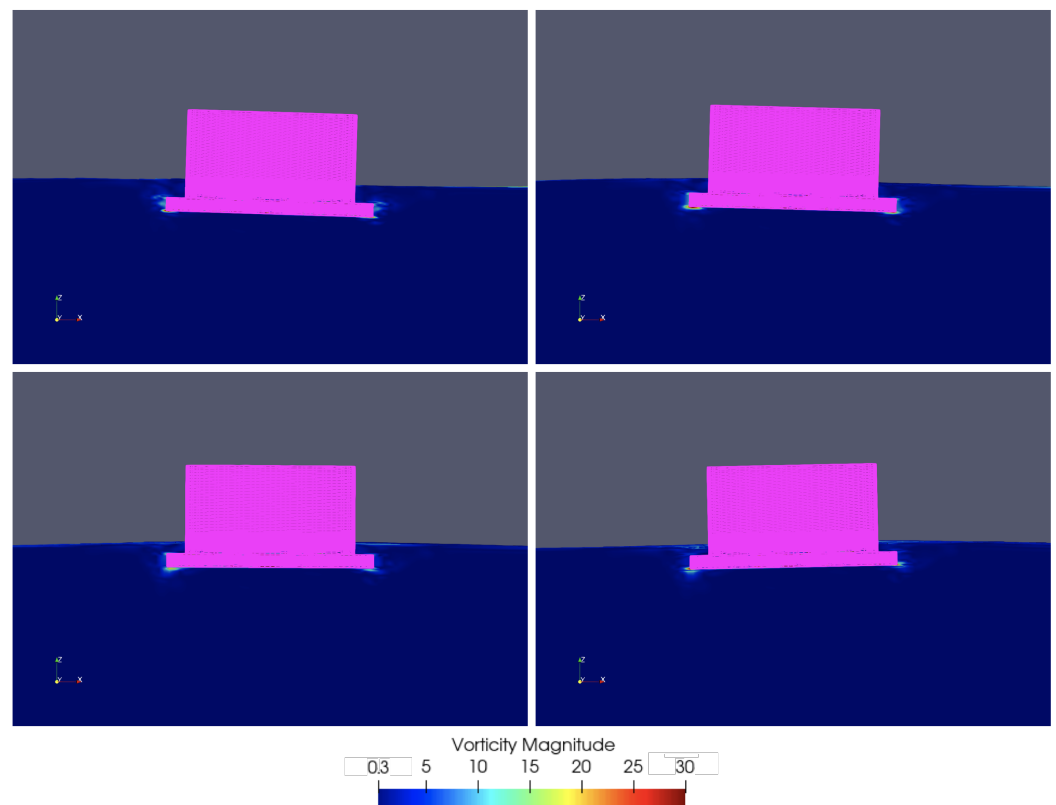
Figure 19. Snapshots of the magnitude of the vorticity near the skirt with $H = 2.72$ cm and $T = 1.4$ s from $t/T = 25.5$ to 26.
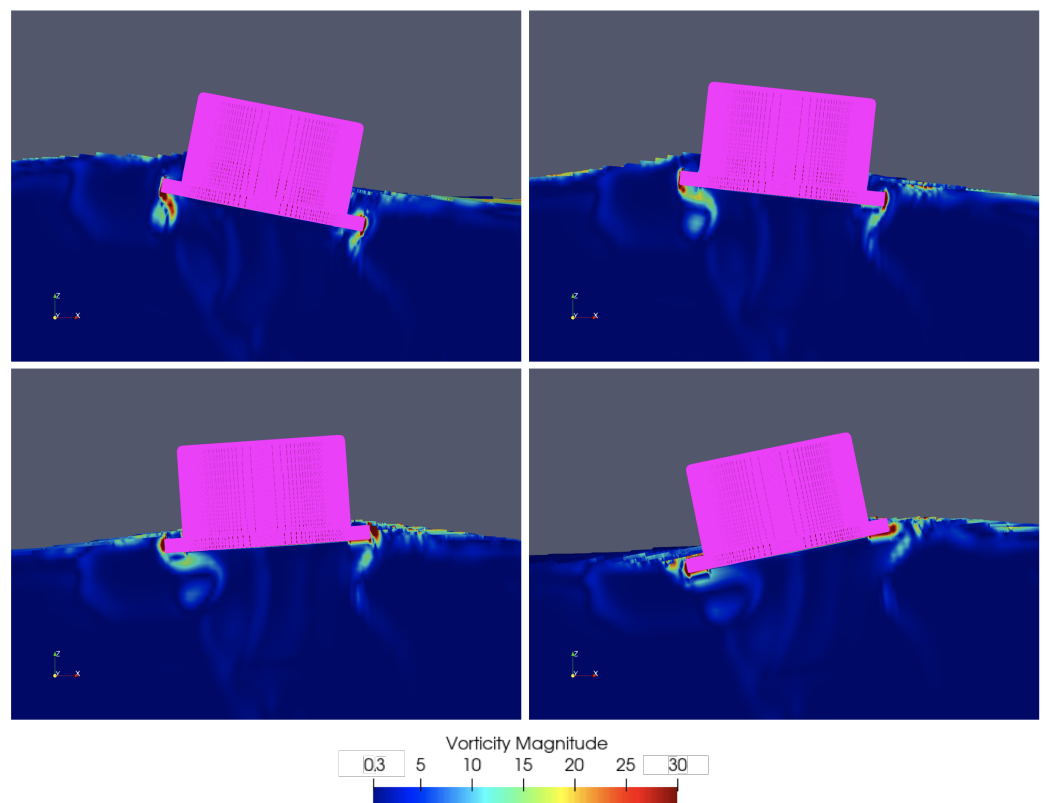

Figure 20. Snapshots of the magnitude of the vorticity near the skirt with $H = 13.6$ cm and $T = 1.4$ s from $t/T = 25.5$ to 26.

In addition, nonlinear restoring forces might cause a further suppressed response for cases in high wave height. Figure 21 illustrates the nonlinear component of the restoring stiffness in the heave direction analyzed according to the area of the water line. The figure shows the increase in the restoring force for a large response (i.e., heave amplitude between 5 to 10 cm) and the decrease for extreme conditions (i.e., heave amplitude greater than 10 cm). Including the effect of this nonlinear restoring stiffness, the equation of motion for heave without coupling can be given by:

$$(M + A_{33})\ddot{x}_3 + B_{1,33}\dot{x}_3 + B_{2,33}\dot{x}_3|\dot{x}_3| + [C_{33} + C_{NL}(x_3, x_5)]x_3 = \text{Re}\left(Fe^{i\omega t}\right), \quad (12)$$

where C_{NL} is the nonlinear component of the restoring force, x_3 is the heave, and x_5 is the pitch displacement, respectively.

The visualization of the water around the floater, Figures 22 and 23, show the the difference of the water line area between $H = 2.72$ cm and $H = 13.6$ cm. As mentioned above, the water line area changes greatly during the oscillation in cases of high wave height, while it makes almost no difference for cases of low wave height.
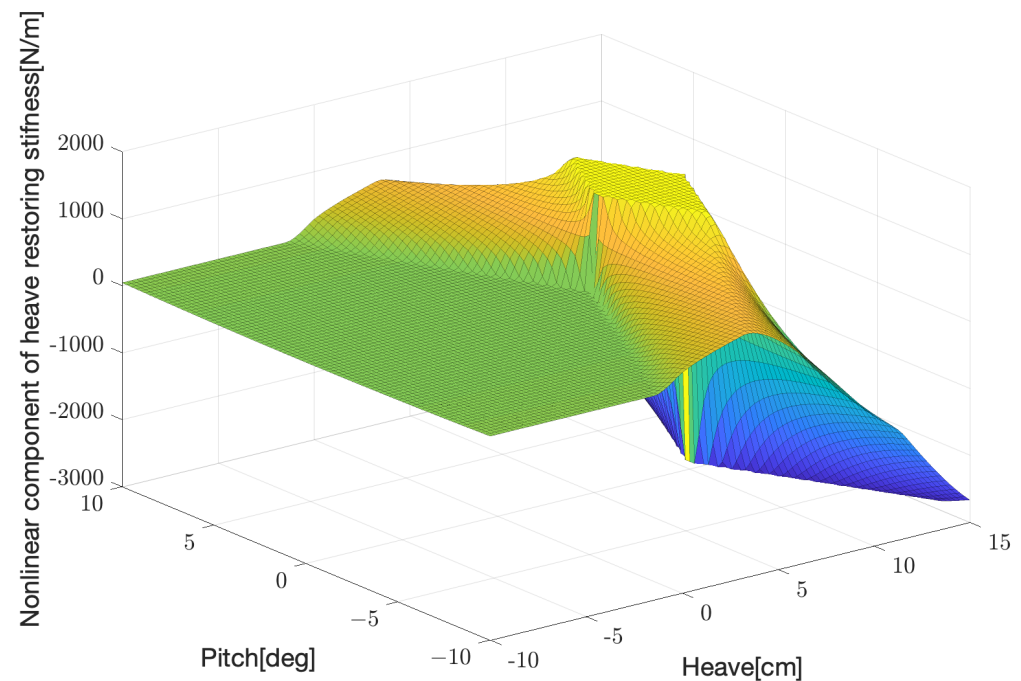

Figure 21. Nonlinear component of the restoring stiffness of heave.

WAMIT simulations with viscous damping $\zeta_{33} = 9.167\%$ showed motion characteristics similar to $H = 6.80$ cm observed in the experiments and the CFD simulations. For the RAOs of pitch, as shown in Figure 18, WAMIT simulations showed completely different motion characteristics from the experiments and CFD simulations. The differences were remarkable around $T = 1.4$ s and the natural period $T \approx 1.7$ s. The reduced pitch motion around the natural period can be explained by the same reasons as for the heave motion, i.e., nonlinear damping. Although constant restoring stiffness is assumed in linear potential theory, the actual restoring stiffness varies depending on the floater's position and rotation. Figure 24 shows the nonlinear component of the restoring stiffness of the floater's pitch motion. As shown in the figure, the restoring stiffness is sensitive to the heave displacement. It is probable that this nonlinear restoring stiffness could change the pitch motion characteristics and could cause the disappearing wave cancellation point at

T = 1.4 s in the experiments and the CFD simulations. Including the effect of this nonlinear restoring stiffness, the equation of motion for heave without coupling can be given by:

$$(I_{55} + A_{55})\ddot{x_5} + B_{1,55}\dot{x_5} + B_{2,55}\dot{x_5}|\dot{x_5}| + [C_{55} + C_{NL}(x_3, x_5)]x_5 = \mathrm{Re}\left(Fe^{i\omega t}\right),\qquad(13)$$

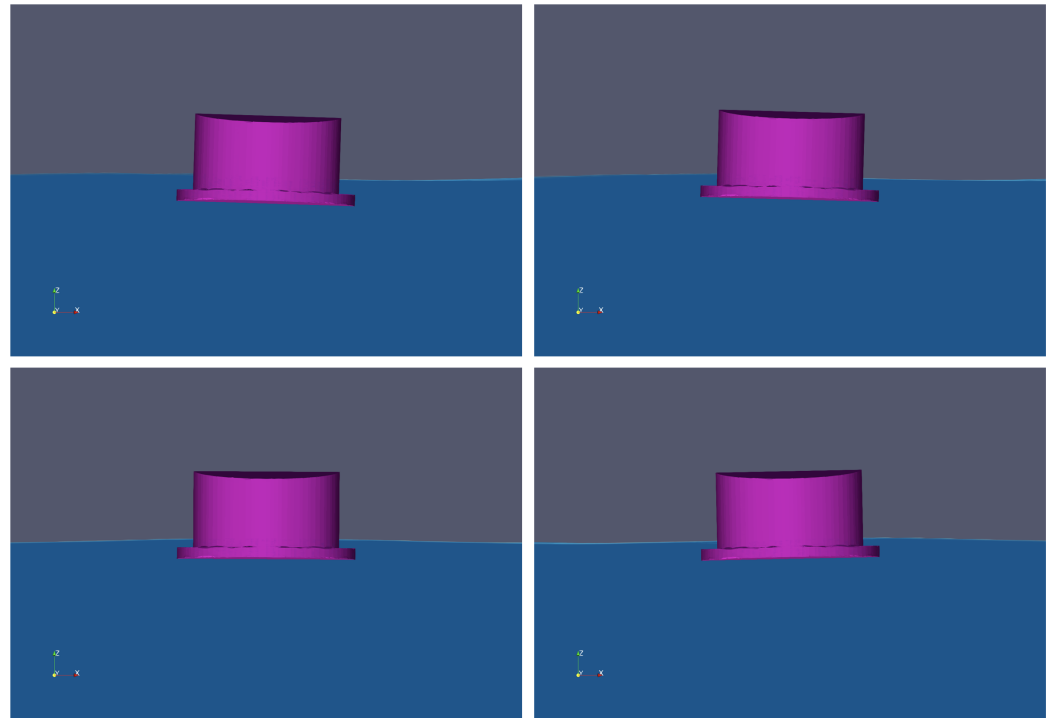where the notations are the same as those used in Equation (12).

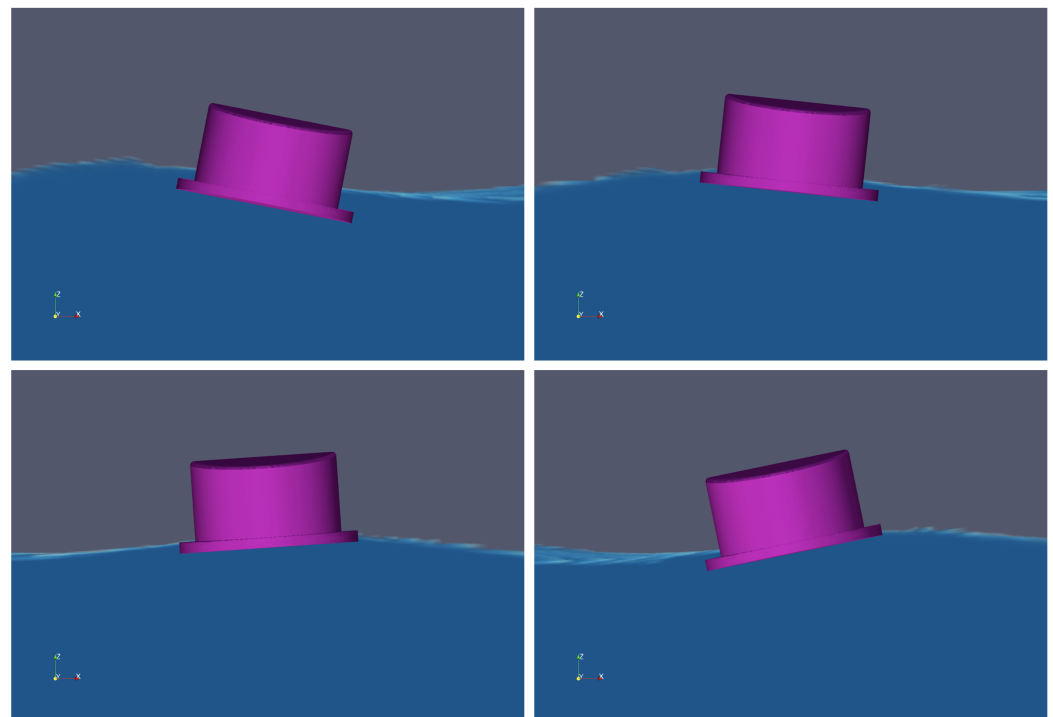**Figure 22.** Snapshots of water and the floater H = 2.72 cm and T = 1.4 s, from t/T = 25.5 to 26.

Figure 23. Snapshots of water and the floater H = 13.6 cm and T = 1.4 s, from t/T = 25.5 to 26.
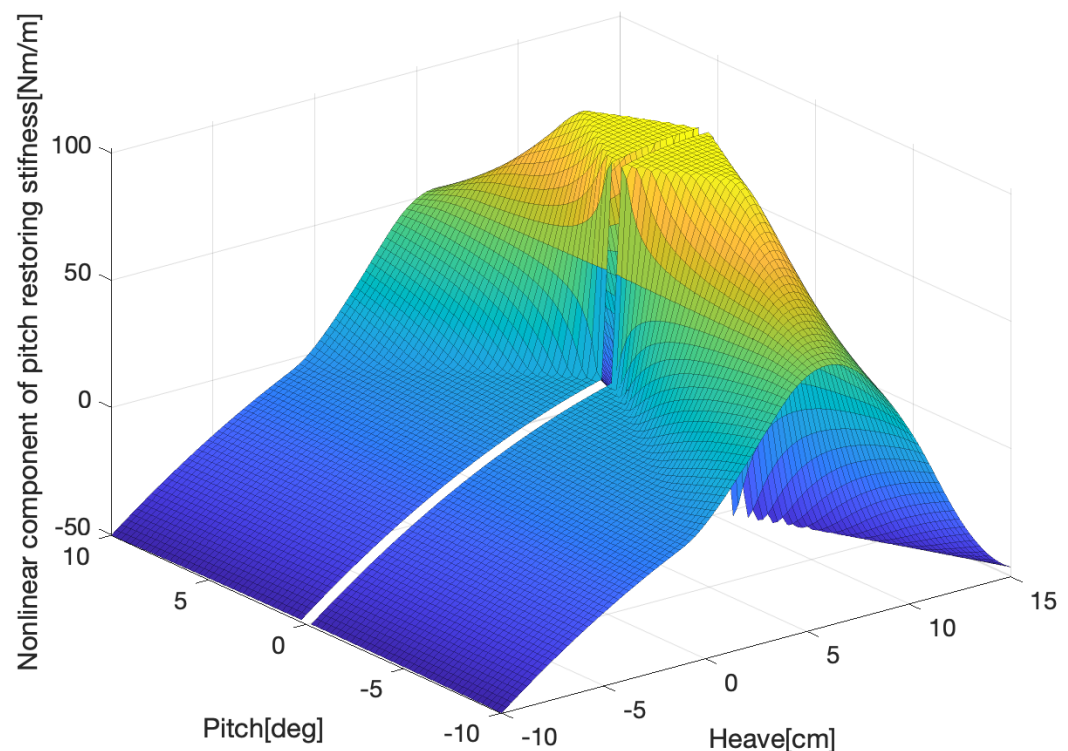
Figure 24. Nonlinear component of the restoring stiffness of pitch.

5. Conclusions

This study investigated the heave and pitch motion characteristics of a monocolumn-type floater with a skirt under regular waves. Wave calibration, free decay, and regular wave tests were performed in the wave tank and CFD simulations. Stable long-term simulations by CFD were enabled by systematic mesh generation.

In the wave calibration tests, the time series of surface elevation was measured, and the wave height was calculated by RMS in both the CFD simulation and the experiment. The time series obtained by the CFD simulations agreed with the theoretical values in all cases. The input wave heights were calibrated in the CFD simulations to reproduce the experimental wave fields. The relative errors of the wave heights between the CFD simulation and the experiment were reduced to less than 1%.

Natural periods and linear and quadratic damping coefficients of heave and pitch motion were calculated for the free decay test, both numerically and experimentally. In addition, a verification and validation study was performed, which showed good agreement between the CFD simulations and the tank experiment.

Regular wave tests were conducted using CFD simulations, potential theory calculations, and tank experiments. RAOs of heave and pitch motion was computed for three wave heights and different wave periods to obtain the motion characteristics. For heave, both the CFD simulations and the potential theory calculations showed good agreement with the experiment. In contrast, the potential theory calculations did not predict the experiment for pitch, while the CFD simulations had excellent accuracy. Visualization of the CFD results showed clear flow separation and significant variations in the waterplane area due to the skirt near the free surface for large oscillation cases. Thus, the nonlinearities observed in the monocolumn with skirt motions were mainly due to the quadratic damping behavior (viscous and vortex-shedding effects) and the abrupt changes in the water line area when heave and pitch motions were large.

In summary, the source of the nonlinearities was the proximity of the skirt and the water line. Designers can obtain the advantages of using skirts as appendages to increase damping and added mass. The nonlinear behavior of the motion equation must be better studied in future works to improve their geometries and position.

Abbreviations

CFD	Computational Fluid Dynamics
BM	metacentric radius
GM	metacentric height
H	wave height
KB	distance from the keel to the center of buoyancy
KG	distance from the keel to the center of gravity
T	wave period
$T_{n,3}$	natural period of heave
$T_{n,5}$	natural period of pitch
RAO	Response Amplitude Operator

Appendix A

Appendix A.1. Linear Damping

A common way to determine the damping of the floater is to perform a free decay test. Consider a linear equation of motion of a point mass in a free decay test:

$$(M + A)\ddot{x} + B_1\dot{x} + Cx = 0, \tag{A1}$$

where M is the mass, A is the added mass, B_1 is the linear damping coefficient, and C is the stiffness. This equation can be written in a non-dimensional form as:

$$\ddot{x} + 2\zeta\omega_n\dot{x} + \omega_n^2 x = 0. \tag{A2}$$

Here ζ is the percentage of critical damping B_{crit} ($\zeta = B_1/B_{crit}$) and ω_n is the natural frequency of the motion. The solution of the above equation is given by the following:

$$x = x_0 e^{-\zeta\omega_n t} \cos\sqrt{1 - \zeta^2}\omega_n t, \tag{A3}$$

where x_0 is the initial condition of the motion. We can obtain an exponential fit curve for the time series of the free decay test as follows:

$$x = a e^{-bt} = x_0 e^{-\zeta\omega_d t}, \tag{A4}$$

where $\omega_d = \sqrt{1 - \zeta^2}\omega_n$ is the damped natural frequency.

Appendix A.2. Quadratic Damping

Studies have shown that the quadratic equation of motion (A5) is more appropriate to represent viscous damping forces.

$$(M + A)\ddot{x} + B_1\dot{x} + B_2\dot{x}|\dot{x}| + Cx = 0, \tag{A5}$$

or in non-dimensional form:

$$\ddot{x} + 2\zeta\omega_n\dot{x} + \frac{B_2}{M + A}\dot{x}|\dot{x}| + \omega_n{}^2 x = 0. \tag{A6}$$

The nonlinear term $\dot{x}|\dot{x}|$ is linearized using the amplitude peaks x_k as follows:

$$\dot{x}|\dot{x}| = \frac{8}{3\pi}x_k\dot{x}. \tag{A7}$$

This linearization gives the following relations between logarithmic decrement and damping coefficients:

$$\frac{1}{2\pi}\ln\frac{x_{k-1}}{x_{k+1}} = \zeta + \frac{4}{3\pi}\frac{B_2}{M + A}x_k. \tag{A8}$$

Equation (A8) is used to determine the values of ζ and B_2 in Section 4.2. Details of this procedure can be found in Malta et al. (2010) [27].

References

1. Public-Private Council on Enhancement of IndustrialCompetitiveness for Offshore Wind Power Generation, Overview of the Vision for Offshore Wind Power Industry (1st). Available online: https://www.enecho.meti.go.jp/category/saving_and_new/saiene/yojo_furyoku/dl/vision/vision_first_overview_en.pdf (accessed on 14 February 2022).
2. Act on Promoting the Utilization of Sea Areas for the Development of Marine Renewable Energy Power Generation Facilities; Law No. 89/2018. Available online: https://policy.asiapacificenergy.org/node/4187 (accessed on 5 August 2022).
3. Ministry of Economy, Trade and Industry, Official Explanation of Technological Standards for Offshore Wind Power Facilities (Revised) Released. Available online: https://www.meti.go.jp/english/press/2020/0327_006.html (accessed on 14 February 2022).
4. Stehly, T.; Duffy, P. *2020 Cost of Wind Energy Review*; NREL/TP-5000-81209; National Renewable Energy Laboratory: Golden, CO, USA, 2021.
5. Chen, J.; Kim, M.H. Review of Recent Offshore Wind Turbine Research and Optimization Methodologies in Their Design. *JMSE* **2022**, *10*, 28. [CrossRef]
6. Yoshimoto, H.; Awashima, Y.; Kitakoji, Y.; Suzuki, H. Development of floating offshore substation and wind turbine for Fukushima FORWARD. In Proceedings of the International Symposium on Marine and Offshore Renewable Energy, Tokyo, Japan, 28–30 October 2013.
7. Matsuoka, R.; Yoshimoto, H. Verification of precision concerning the design of advanced spar type structure. *JASNAOE* **2015**, *20*, 1–4.
8. Gonçalves, R.T.; Matsumoto, F.T.; Malta, E.B.; Medeiros, H.F.; Nishimoto, K. Conceptual Design of Monocolumn Production and Storage With Dry Tree Capability. *J. Offshore Mech. Arct. Eng.* **2010**, *132*, 041301. [CrossRef]
9. Gonçalves, R.T.; Matsumoto, F.T.; Malta, E.B.; Rosetti, G.F.; Fujarra, A.L.C.; Nishimoto, K. Evolution of the MPSO (monocolumn production, storage and offloading system). *Mar. Syst. Ocean Technol.* **2010**, *5*, 45–53. [CrossRef]
10. Wang, W.H.; Wang, L.L.; Du, Y.Z.; Yao, Y.X.; Huang, Y. Numerical and experimental analysis on motion performance of new sandglass-type floating body in waves. *Mar. Struct.* **2016**, *46*, 56–77. [CrossRef]
11. Du, Y.Z.; Wang, W.H.; Wang, L.L.; Huang, Y. Nonlinear dynamics of heave motion of the sandglass-type floating body with piecewise-nonlinear, time-varying stiffness. *Mar. Struct.* **2018**, *60*, 136–150. [CrossRef]
12. Amin, I.; Dai, S.; Oterkus, S.; Day, S.; Oterkus, E. Experimental investigation on the motion response of a novel floating desalination plant for Egypt. *Ocean Eng.* **2020**, *210*, 107535. [CrossRef]
13. Rao, M.J.; Nallayarasu, S.; Bhattacharyya, S.K. CFD approach to heave damping of spar with heave plates with experimental validation. *APOR* **2021**, *108*, 102517. [CrossRef]
14. Jang, H.K.; Kim, M.H. Effects of nonlinear FK (Froude-Krylov) and hydrostatic restoring forces on arctic-spar motions in waves. *IJNAOE* **2020**, *12*, 297–313. [CrossRef]
15. Beyer, F.; Arnold, M.; Cheng, P.W. Analysis of Floating Offshore Wind Turbine Hydrodynamics Using coupled CFD and Multibody Methods. In Proceedings of the Twenty-Third (2013) International Offshore and Polar Engineering, Anchorage, AK, USA, 30 June–5 July 2013.

16. Quallen, S.; Xing, T. CFD simulation of a floating offshore wind turbine system using a variable-speed generator-torque controller. *Renew. Energy* **2016**, *97*, 230–242. [CrossRef]
17. Borisade, F.; Choisnet, T.; Cheng, P.W. Design study and full scale MBS-CFD simulation of the IDEOL floating offshore wind turbine foundation. *JPCS* **2016**, *753*, 092002. [CrossRef]
18. Xue, M.A.; Dou, P.; Zheng, J.; Lin, P.; Yuan, X. Pitch motion reduction of semisubmersible floating offshore wind turbine substructure using a tuned liquid multicolumn damper. *Mar. Struct.* **2022**, *84*, 103237. [CrossRef]
19. Wang, Y.; Chen, H.C.; Vaz, G.; Mewes, S. CFD Simulation of Semi-Submersible Floating Offshore Wind Turbine Under Pitch Decay Motion. In Proceedings of the ASME 2019 2nd International Offshore Wind Technical Conference IOWTC2019, St. Julian's, Malta, 3–6 November 2019.
20. Wang, Y.; Chen, H.C.; Vaz, G.; Mewes, S. CFD Simulation of Semi-Submersible Floating Offshore Wind Turbine under Regular Waves. In Proceedings of the 30th International Ocean and Polar Engineering Conference, Virtual, 11–16 October 2020.
21. Suzuki, H.; Sakai, Y.; Yoshimura, Y.; Houtani, H.; Carmo, L.H.S.; Yoshimoto, H.; Kamizawa, K.; Conçalves, R.T. Non-Linear Motion Characteristics of a ShallowDraft Cylindrical Barge Type Floater for a FOWT in Waves. *JMSE* **2021**, *9*, 56. [CrossRef]
22. Menter, F.R.; Egorov, Y. Development and applicationof SST-SAS turbulence model in the DESIDER project. In *Advances in Hybrid RANS-LES Modeling*; Peng, S.H., Haase, W., Eds.; Springer: Berlin/Heidelberg, Germany, 2007; pp. 261–270.
23. Burmester, S.; Vaz, G.; Moctor, O.E.; Gueydon, S.; Koop, A.; Chen, H.C. High-Fidelity Modelling of Floating Offshore Wind Turbine Platforms. In Proceedings of the 39th International Conference on Ocean, Offshore & Arctic Engineering OMAE 2020, Fort Lauderdale, FL, USA, 28 June–3 July 2020.
24. Menter, F.R.; Egorov, Y. The Scale-Adaptive Simulation Method for Unsteady Turbulent Flow Predictions Part 1: Theory and Model Description. *Flow Turbul. Combust* **2010**, *85*, 113–138. [CrossRef]
25. ITTC Quality Manual. ITTC—Recommended Procedures and Guidelines: Uncertainty Analysis in CFD Verification and Validation, Methodologies and Procedures (7.5-03-01-01), 2017. Available online: https://www.ittc.info/media/8153/75-03-01-01.pdf (accessed on 8 September 2022).
26. Rosetti, G.F. Improvements in the Numerical Modeling of Turbulence and Fluid-Structure Interaction for the Vortex-Induced Vibrations of a Rigid Cylinder. Ph.D. Thesis, The University of São Paulo, São Paulo, Brazil, 2015.
27. Malta, E.B.; Gonçalves, R.T.; Matsumoto, F,T.; Pereira, F.R.; Fujarra, A.L.C.; Nishimoto, K. Damping coefficient analysis for floating offshore structures. In Proceedings of the ASME 2010 29th International Conference of Offshore Mechanics and Arctic Engineering, OMAE2010-20093, Shanghai, China, 6–11 June 2010.